metals

MDPI

Article

Effects of Residual Stress on Springback in Creep Age Forming of 2219 Aluminum Alloy Double-Curvature Thin-Walled Parts

Jiwang Yu [1], Lihua Zhan [1,2] and Youliang Yang [1,2,*]

[1] Light Alloy Research Institute, Central South University, Changsha 410083, China; cosine.csu.edu@gmail.com (J.Y.); yjs-cast@csu.edu.cn (L.Z.)
[2] State Key Laboratory of Precision Manufacturing for Extreme Service Performance, Central South University, Changsha 410083, China
* Correspondence: yangyouliang@csu.edu.cn

Abstract

Residual stresses are inevitably introduced during plate manufacturing and pre-processing (e.g., quenching and pre-stretching). However, springback prediction in creep age forming (CAF) is still frequently carried out by assuming an initially stress-free blank, which may lead to biased deformation–stress histories and tool compensation errors, hindering high-accuracy forming. This study aimed to close this practical gap by quantifying how inherited residual stresses affected the CAF springback of AA2219 double-curvature thin-walled parts. In this study, a multi-step finite element (FE) process chain covering quenching, pre-stretching, and creep age forming (CAF) was developed to investigate the evolution of the initial residual stress field and its influence on CAF springback. Surface residual stresses after quenching and after pre-stretching were measured by X-ray diffraction (XRD) to validate the FE models. The results show that, after quenching, the through-thickness residual stress exhibits a characteristic 'compressive at the surfaces and tensile in the core' distribution, and pre-stretching markedly reduces the residual stress level. During CAF, although the initial residual stress difference is largely equilibrated during loading, it affects springback primarily through differences in accumulated creep deformation. Incorporating the initial residual stress field reduces the springback error bandwidth from 9.59 mm to 3.51 mm (a 63.4% reduction) under the original die configuration. Additional simulations under a modified die curvature (geometric deviation ≈ 6 mm) demonstrate that the springback reduction remains at the millimeter scale, indicating that the proposed FE framework maintains a consistent predictive improvement across different curvature conditions. This work provides a theoretical basis and practical guidance for high-precision creep age forming.

Keywords: aluminum alloy; creep age forming; initial residual stress; springback

Check for updates

Academic Editor: Jiri Svoboda

Received: 2 February 2026
Revised: 24 February 2026
Accepted: 26 February 2026
Published: 28 February 2026

Copyright: © 2026 by the authors. Licensee MDPI, Basel, Switzerland. This article is an open access article distributed under the terms and conditions of the Creative Commons Attribution (CC BY) license.

1. Introduction

Creep age forming (CAF) is an advanced manufacturing technology that couples creep deformation with age hardening, enabling the high-accuracy forming of large and complex panels. It has been widely applied in aerospace structures such as wing skins and fuselage panels [1–4]. However, because the internal stresses in loaded parts cannot be fully relaxed during CAF, springback is unavoidable [5–7]. Therefore, the accurate prediction of springback in CAF is a prerequisite for high-precision forming.

Over the past few decades, numerous studies have characterized creep ageing behavior and established constitutive models, which have been implemented in finite element

simulations to predict deformation and springback during CAF [8–10]. In addition, the initial residual stresses introduced during pre-processing can also significantly affect springback. It has been reported that machining-induced surface residual stresses alter the stress superposition during CAF, thereby changing the final springback [11–13]. Beyond machining, the pre-processing steps before forming—such as quenching and pre-stretching—also play an important role in determining residual stress distributions [14–17], yet systematic studies on their effects on CAF springback remain limited.

More broadly, the coupling among surface integrity, residual stress states, and the subsequent mechanical response has been widely recognized in adjacent manufacturing and surface engineering processes. For instance, the green electrochemical polishing of additively manufactured Ti6Al4V has been shown to reshape the surface condition and to correlate strongly with the residual stress-sensitive fatigue response [18]. In cold-spray processing, numerical studies of rebound phenomena emphasize that transient stress evolution governs rebound/bonding outcomes, which provides a methodological context for stress evolution-driven "springback-like" behaviors [19]. Moreover, surface laser texturing prior to cold spraying can markedly influence deposition outcomes, highlighting the general importance of the initial surface/near-surface states across processes [20]. These cross-process findings further highlight the need to systematically account for inherited residual stresses in CAF springback prediction.

Residual stress measurement provides the most direct means to obtain stress distributions. Mechanical methods (e.g., hole drilling and sectioning) evaluate residual stresses by releasing strains but are destructive to the component [21–24]. Diffraction-based methods (e.g., X-ray and neutron diffraction) infer stresses from diffraction peak shifts and are non-destructive [25]. However, X-ray diffraction typically probes only the near-surface region (in the order of micrometers) [25,26], whereas neutron diffraction can access deeper regions but is costly and not widely available [27–29]. Therefore, a full-process-chain FE simulation from quenching and pre-stretching to CAF is of great engineering value in evaluating the overall residual stress field and its effects on springback.

In this work, a large AA2219-C10Z propellant tank panel (gore) is taken as the target component. A multi-step FE process chain of quenching–pre-stretching–CAF is established and validated by experiments. The residual stress distribution after quenching and pre-stretching is analyzed, and the influence of the resulting initial residual stresses on the forming accuracy of a doubly curved component is investigated. Section 2 describes the residual stress measurements and CAF experiments. Section 3 introduces the multi-step FE models. Section 4 presents and discusses the simulation results and experimental validation, clarifying the residual stress characteristics and their mechanisms affecting springback.

2. Experiments

A full process chain was represented by coupling multiple FE models, as schematically shown in Figure 1. The residual stress field predicted by the quenching model was imported as the initial stress state for the pre-stretching model; the resulting stress field after pre-stretching was then used as the initial stress state for the CAF model. To ensure reliability, surface residual stresses predicted at each stage were compared with experimental measurements.

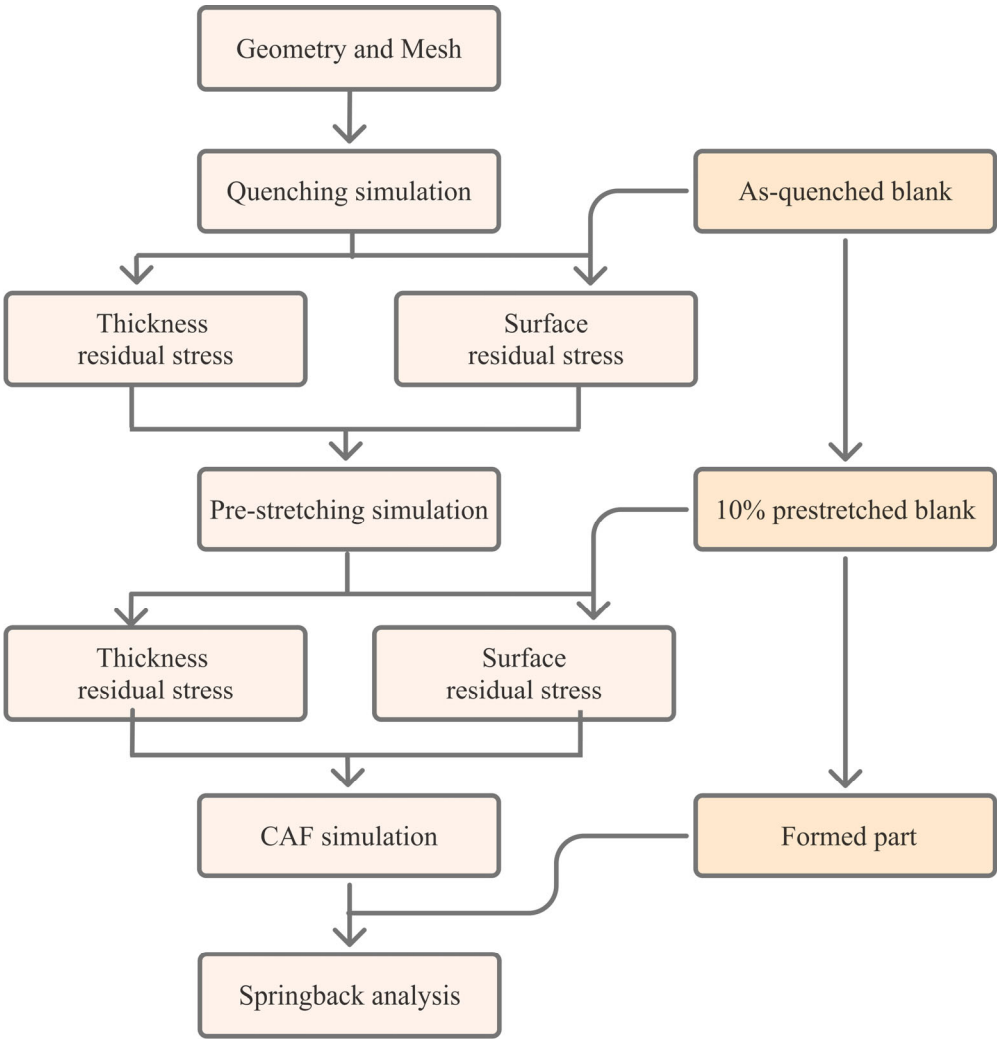


Figure 1. Schematic showing the detailed modeling routes in this study.

2.1. Residual Stress Measurement

The material used was a hot-rolled AA2219 plate (chemical composition listed in Table 1). The surface residual stresses of the solution-treated (quenched) and C10Z (quenched + 10% pre-stretch) plates were measured by X-ray diffraction (XRD) using a portable X-ray residual stress diffractometer (Proto iXRD, Proto Manufacturing Ltd., Windsor, ON, Canada), as shown in Figure 2a.

Table 1. Chemical composition of hot-rolled AA2219 plate (wt.%).

Cu	Mg	Mn	Si	Fe	Ni	Zr	Ti	Al
5.24	0.028	0.27	0.042	0.13	0.03	0.14	0.065	Bal.

To ensure measurement reliability, the measured areas were pre-treated prior to XRD testing to minimize the influences of oxide layers and surface roughness on the diffraction quality. The surface oxide layer was first removed by gentle mechanical polishing using fine-grade abrasive paper. Subsequently, light polishing was performed to obtain a smooth and uniform surface. During the preparation process, special care was taken to avoid introducing additional mechanical deformation or residual stresses. After polishing, the surfaces were cleaned with ethanol to remove debris and contaminants.

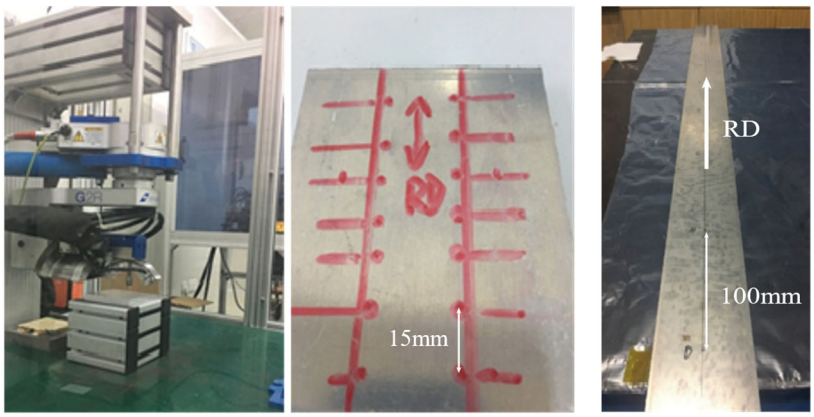


Figure 2. Residual stress measurement: (**a**) XRD instrument; (**b**) quenched plate; (**c**) quenched and pre-stretched plate. Surface residual stresses were measured by XRD for both conditions.

A 100 × 100 mm plate with a thickness of 12 mm was solution-treated at 535 °C for 48 min and then water-quenched. Seven measurement points were selected at equal spacing along the rolling direction. Each point was measured twice at two adjacent locations separated by 15 mm, and the average value was used for comparison with the simulation results (Figure 2b).

For the quenched-and-pre-stretched plate (AA2219-C10Z, i.e., 10% pre-stretch after quenching), a 100 × 1200 mm specimen with a thickness of 12 mm was prepared. Ten points were selected at 100 mm intervals along the rolling direction (Figure 2c), and surface residual stresses were measured in both the rolling and transverse directions.

Residual stresses were determined using the standard $\sin^2\psi$ method, which evaluates stress from the linear relationship between lattice strain and $\sin^2\psi$. A diffraction plane appropriate for aluminum alloys was selected according to standard laboratory practice. Multiple ψ tilt angles were applied to ensure reliable linear fitting of the diffraction peak shifts. The scanning parameters, including the ψ range, angular step size, and counting time, were chosen to provide sufficient peak resolution and statistical stability consistent with conventional laboratory XRD residual stress measurements.

The XRD system was routinely calibrated using stress-free reference samples prior to measurement. The repeatability of measurements was verified by repeated testing at selected locations, and the variation between repeated measurements remained within the typical uncertainty range of laboratory XRD residual stress analysis. These procedures ensured the reliability of the experimental data used for the validation of the finite element models.

2.2. Creep Age Forming Experiment

To validate the influence of the initial residual stress field on subsequent CAF springback, a creep age forming experiment was performed on a doubly curved component. The target part was an ellipsoidal shell panel (Figure 3a) and the blank was an isosceles trapezoidal plate with the following dimensions: long side 1455 mm, short side 644 mm, height 2497 mm, and thickness 12 mm (Figure 3b). The material was AA2219-C10Z.

Loading was applied at room temperature by pneumatic pressure. The procedure was as follows: first, the plate was pre-loaded by vacuum-assisted sealing (0.1 MPa; Figure 4a); then, the tooling assembly was transferred into an autoclave (Xi'an Longde Co., Ltd., Xi'an, China) (Figure 4b) and pressurized to 1 MPa; next, ageing under pressure was conducted at 165 °C for 8 h; finally, the pressure was released to obtain the springback component (Figure 4c).

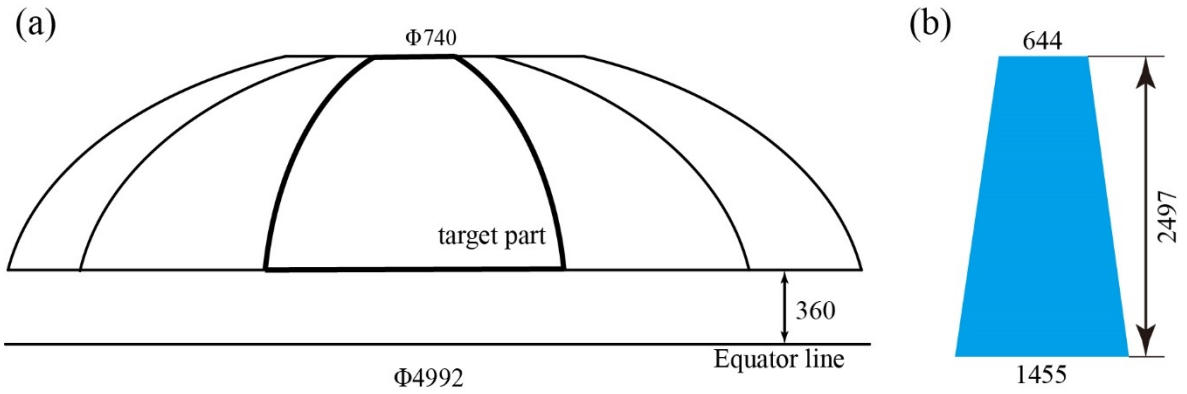


Figure 3. Dimensions: (**a**) target part, (**b**) blank.

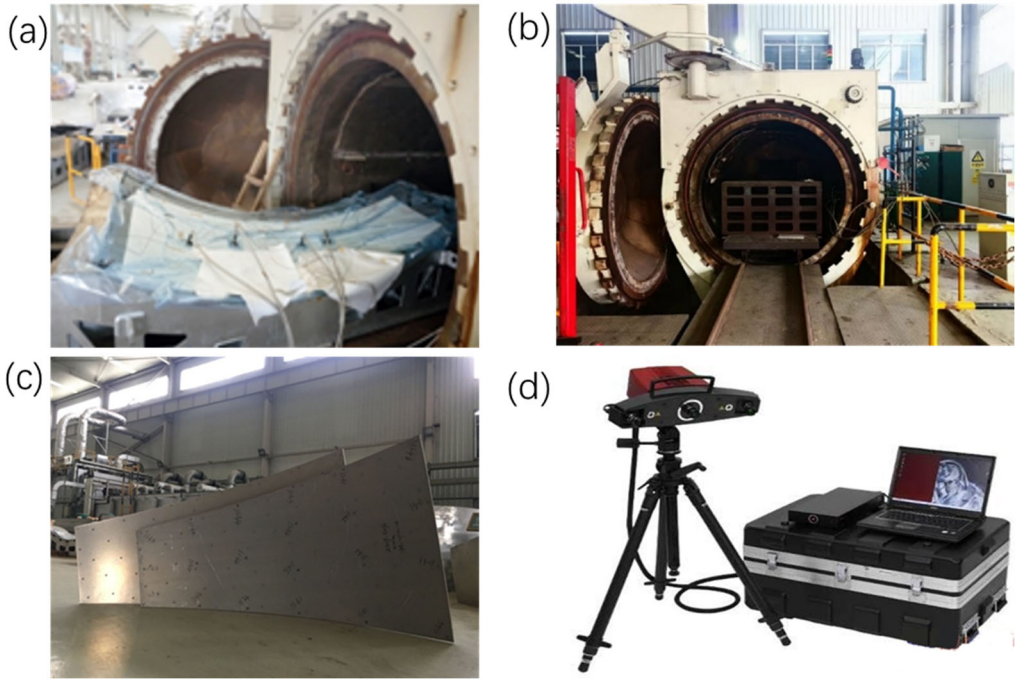


Figure 4. Creep age forming experiment: (**a**) vacuum sealing; (**b**) autoclave; (**c**) formed component after unloading; (**d**) surface profile scanner.

The surface profile of the formed component was measured using a non-contact three-dimensional surface scanning system (ATOS 3D optical scanner, GOM GmbH, Braunschweig, Germany) (Figure 4d). Prior to scanning, the specimen was placed on a stable reference platform to minimize rigid-body movement. Multiple scans were performed and merged to ensure full-field coverage of the doubly curved surface. The point cloud data were processed using GOM Inspect 2018 software (GOM GmbH, Braunschweig, Germany).

To evaluate springback, the measured surface was aligned with the target CAD geometry using a best fit algorithm based on least squares minimization. Rigid-body translations and rotations were removed during the alignment process to eliminate positioning errors. The geometric deviation between the scanned surface and the target shape was then calculated in the normal direction of the reference surface. The same alignment procedure was applied to both experimental and FE-predicted geometries to ensure consistency and reduce systematic errors.

3. Finite Element Modeling Considering Residual Stress

A multi-step thermomechanical finite element (FE) process chain was established to simulate quenching, pre-stretching, and subsequent creep age forming (CAF). All simulations were performed using MSC.Marc 2020 (MSC Software LLC, Newport Beach, CA, USA), which allows fully coupled thermomechanical analysis and user-defined material subroutines.

Three sequential FE models were constructed: (i) a quenching model, (ii) a pre-stretching model, and (iii) a creep age forming (CAF) model. The residual stress field obtained at the end of each stage was transferred as the initial stress state to the subsequent model to maintain process continuity.

3.1. Quenching and Pre-Stretching Model

Finite element simulations of solution quenching and subsequent pre-stretching were performed for the AA2219 plate to investigate the residual stress distribution induced by quenching (Figure 5). The model size was 100 mm × 100 mm × 12 mm. A hexahedral mesh was used, with an element size of 2 mm through the thickness and 5 mm in the length and width directions. The initial temperature was set to 535 °C and the quenching medium temperature to 20 °C.

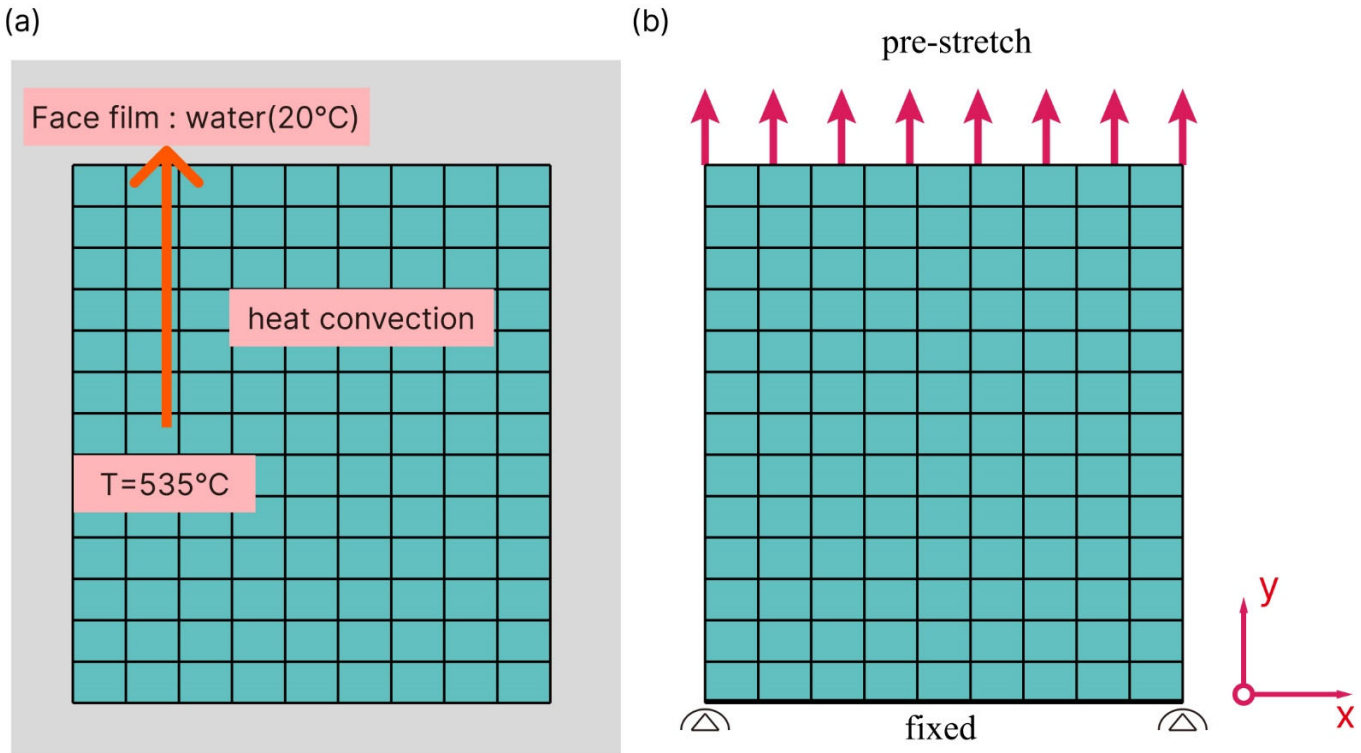


Figure 5. Finite element models for residual stress evaluation: (**a**) quenching; (**b**) pre-stretching. Arrows indicate heat convection in (**a**) and pre-stretching direction in (**b**); triangles in (**b**) denote fixed boundaries.

The mechanical properties were obtained from repeated tensile tests, as shown in Figure 6.

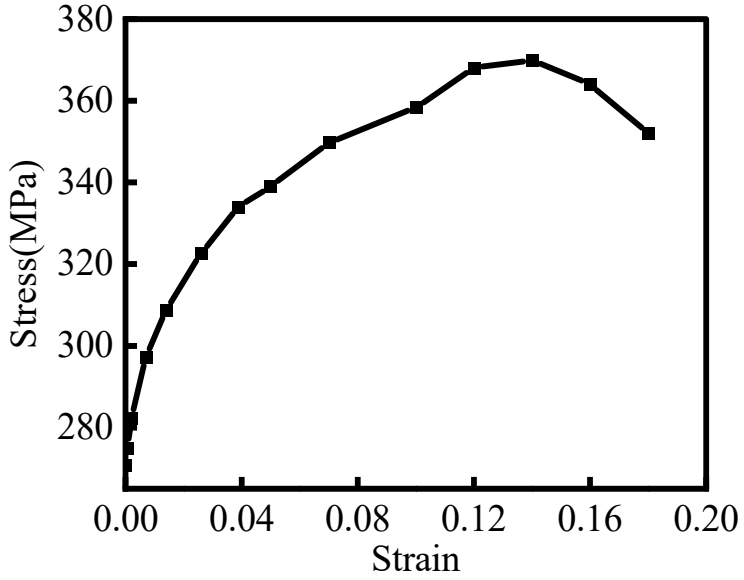


Figure 6. Stress–strain curve of AA2219 at room temperature.

In the thermomechanical coupled quenching simulation, the key thermophysical parameters of AA2219 included the thermal conductivity, specific heat capacity, Young's modulus, Poisson's ratio, and convective heat transfer coefficient. Their temperature dependencies are shown in Figure 7. The effect of the quench medium temperature rise on the heat transfer coefficient was neglected. Quenching heat transfer was treated as forced convection with a convective coefficient of 20 $mW \cdot mm^{-2} \cdot {}^{\circ}C^{-1}$, and the remaining parameters were taken from the literature [22].

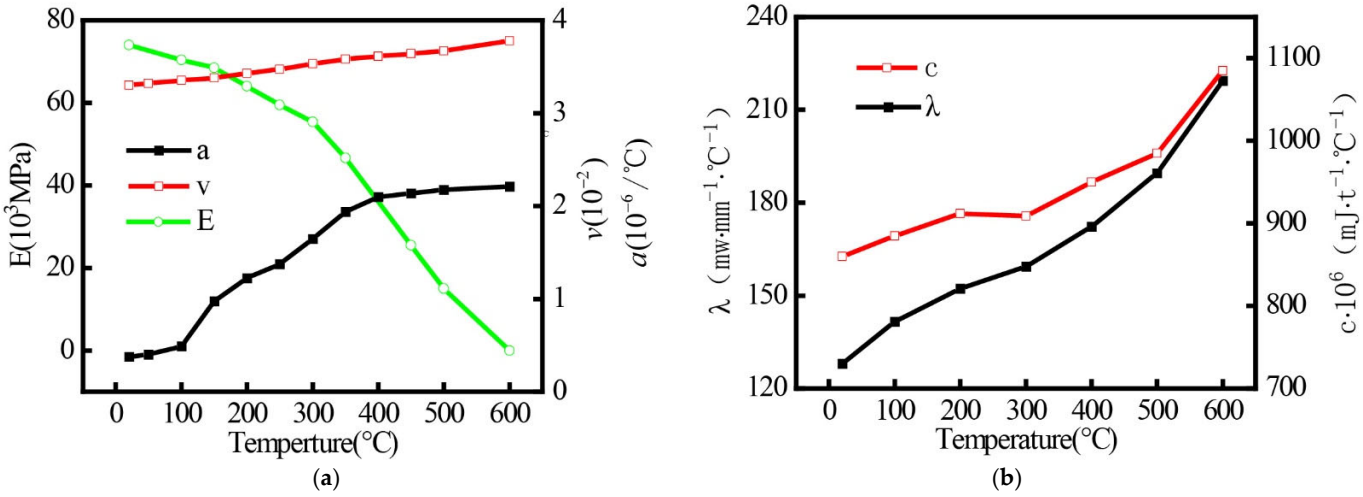


Figure 7. Temperature-dependent material properties: (**a**) elastic modulus E, Poisson's ratio ν, and coefficient of linear thermal expansion α; (**b**) thermal conductivity and specific heat capacity.

The residual stress field at the end of quenching was imported as the initial stress state for the pre-stretching simulation. Nodes at one end of the plate were fixed, and displacement corresponding to 10% tensile strain was applied at the opposite end to simulate pre-stretching (Figure 5b).

3.2. Creep Age Forming Model

3.2.1. Geometry and Mesh

Figure 8 shows the FE model for the creep age forming of a doubly curved thin-walled AA2219 component. To accurately capture the through-thickness stress/strain gradients,

an 8-node hexahedral mesh was adopted. The in-plane mesh size was 10 mm × 10 mm, while six elements were assigned through the thickness (2 mm per layer), resulting in total thickness discretization of 12 mm. The die surface was modeled as a rigid body, and the friction coefficient between the plate and die was set to 0.3.

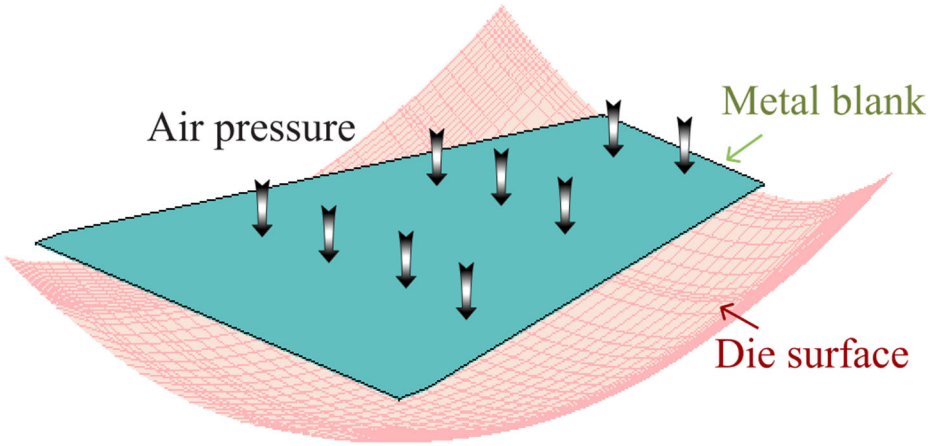


Figure 8. FE model for creep age forming of a doubly curved thin-walled component.

The initial residual stress field obtained from the quenching and pre-stretching simulations was imported into the CAF model using the user subroutine UINSTR, which allows pre-defined stress initialization at the start of the simulation step; this model is referred to as the RS model. For comparison, a model without initial residual stress was used, referred to as the NRS model.

The CAF simulation consisted of three stages. In the loading stage (static step), the pneumatic pressure was represented by uniformly distributed normal compressive stress on the plate surface, ramped linearly from 0 to 1 MPa within 1 h. The creep ageing stage then maintained the pressure for 8 h. Finally, the pressure was released to obtain the springback configuration.

To evaluate the robustness of the FE model with respect to the tooling curvature, an additional simulation was conducted using a shallower die surface. The maximum geometric deviation between the shallow die and the experimental die surface was 6 mm.

3.2.2. Creep Constitutive Model

Based on creep ageing tests of AA2219-C10Z and the unified constitutive framework, a macro–micro constitutive model was established to predict springback deformation and the ageing response, as follows:

$$\dot{\varepsilon_c} = A \cdot sinh\left\{ \frac{B \cdot (\sigma - \sigma_0) \cdot (1 + k_1 \overline{\rho})}{\sigma_y} \right\}^{m_1} \tag{1}$$

$$\sigma_y = \sigma_i + \sigma_{ss} + \sigma_{ppt} + \sigma_{dis} \tag{2}$$

$$\sigma_{\mathrm{ss}} = C_{\mathrm{ss}} \cdot \left(1 - \overline{f_v}\right)^{2/3} \tag{3}$$

$$\sigma_{\mathrm{ppt}} = c_{ppt} \cdot \overline{f_v}^{1/2} \cdot q^{\mathrm{n}_1} \tag{4}$$

$$\sigma_{dis} = C_{dis} \cdot \overline{\rho}^{n_2} \tag{5}$$

$$\dot{\overline{f_v}} = \frac{C_1 \cdot l^3 \cdot \dot{l}}{q} \left(1 - \overline{f_v}\right)^{m_2} \cdot (1 + k_2 \cdot \overline{\rho}^{n_3}) \tag{6}$$

$$\dot{l} = C_2 \cdot (\mathrm{a} + \mathrm{b} \cdot \sigma - l)^{m_3} \cdot (1 + k_3 \cdot \overline{\rho}^{n_4}) \tag{7}$$

$$q = C_3 \cdot \left(exp\left[-k_4 (t - t^*)^2 \right] - \sigma^{n_5} \right) \cdot t^{n_6} + 1 \tag{8}$$

$$\dot{\bar{\rho}} = -C_4 \cdot \bar{\rho} \cdot \left| \dot{\varepsilon_c} \right| \tag{9}$$

where the symbols (e.g., ξ) are the material parameters of the constitutive model, as listed in Table 2. The constitutive equations were implemented in MSC.Marc 2020 through the user material subroutine CRPLAW, which enables user-defined creep laws and internal variable evolution.

Table 2. Constitutive parameters for creep ageing of AA2219-C10Z.

Parameter	Value	Parameter	Value	Parameter	Value
A/h^{-1}	0.9533	C_3	141.9358	n_4	4.6796
B/MPa^{-1}	0.1420	C_4	271.8296	n_5	0.1744
σ_0/MPa	15.3682	k_1	1.6252	n_6	0.1
σ_i/MPa	111.2442	k_2	0.3753	m_1	3.1997
C_{ss}/MPa	70.3445	k_3	0.5569	m_2	0.5459
C_{ppt}/MPa	79.0815	k_4	0.0102	m_3	0.6015
C_{dis}/MPa	125.0606	n_1	0.2217	a	94.05
C_1	3.701×10^{-6}	n_2	0.0497	b	−0.115
C_2	1.0000	n_3	4.9997	t^*	11

3.2.3. Mesh Convergence Analysis

To verify the numerical stability and reliability of the finite element model, a mesh convergence study was carried out for the creep age forming simulation. Particular attention was given to through-thickness discretization, as it is essential in accurately capturing the stress and strain gradients that govern springback behavior.

Three mesh configurations were examined, employing 4, 6, and 8 solid elements through the thickness while maintaining an identical in-plane mesh density. The predicted springback values for the three discretization cases are summarized in Table 3.

Table 3. Mesh convergence study for springback prediction.

Through-Thickness Elements	4	6	8
Springback (mm)	85.56	88.30	88.28

The results show that increasing the number of through-thickness elements from six to eight leads to a negligible change in springback (88.30 mm vs. 88.28 mm), indicating numerical convergence. Although the four-layer mesh yields a slightly lower value (85.56 mm), the difference between the six- and eight-layer models is minimal relative to the overall deformation magnitude.

Considering a balance between computational efficiency and numerical accuracy, the discretization of six elements through the thickness was selected for all subsequent simulations.

4. Results and Discussion

4.1. Surface Residual Stress

Figure 9 compares the measured and simulated surface residual stresses after quenching. Along the rolling direction, the measured average residual stress was −138.7 MPa; the maximum deviation between the simulation and experiment was 13 MPa, corresponding to a 9.1% difference. Along the transverse direction, the measured average was 140.1 MPa; the maximum deviation was 9 MPa, corresponding to a 6.7% difference. Therefore, the quenching FE model can be considered to capture the thermo-stress evolution during quenching with good accuracy.

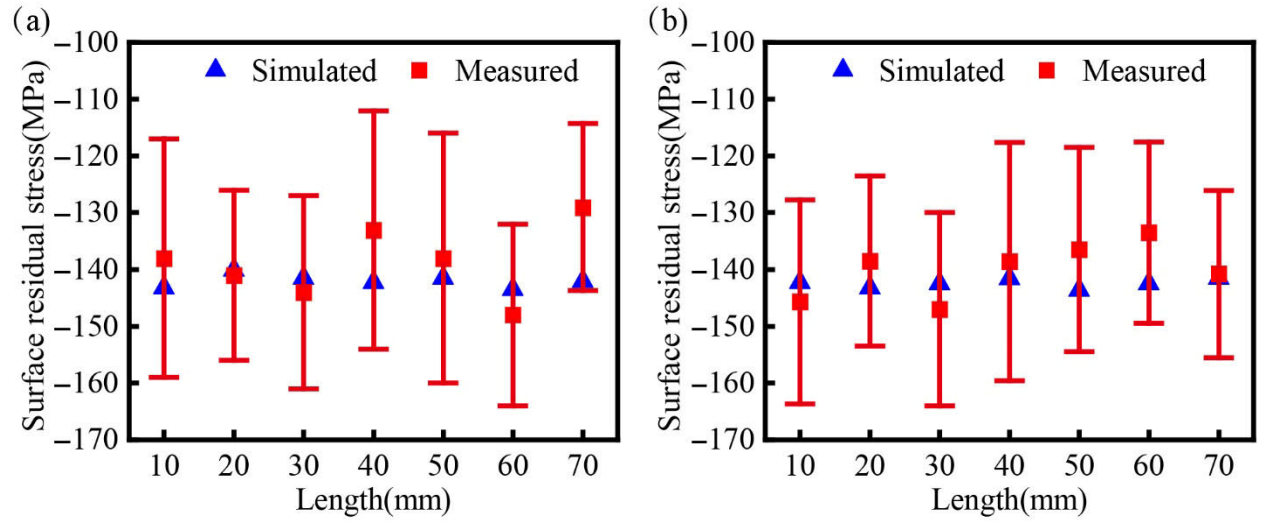


Figure 9. Simulated and measured surface residual stresses after quenching: (**a**) rolling direction; (**b**) transverse direction.

Figure 10 compares the simulated and measured surface residual stresses after pre-stretching. The simulated average residual stress was −36.6 MPa in the rolling direction and −33.4 MPa in the transverse direction. The measured averages were −32.3 MPa (rolling) and −30.6 MPa (transverse), with maximum deviations of 7.8 MPa and 5.1 MPa, respectively. These results indicate that the pre-stretching FE model is reliable.

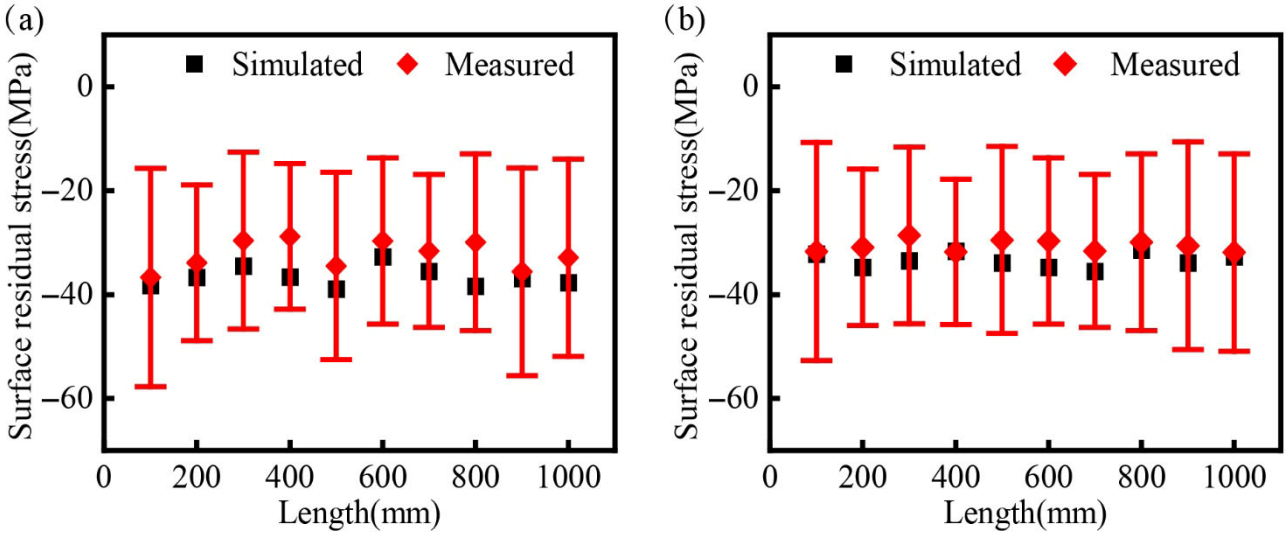


Figure 10. Simulated and measured surface residual stresses after quenching and pre-stretching: (**a**) rolling direction; (**b**) transverse direction.

4.2. Through-Thickness Residual Stress

Figure 11 shows the simulated through-thickness residual stress distributions after quenching and after pre-stretching. The residual stress is symmetric about the mid-plane and exhibits a characteristic 'compressive at the surfaces and tensile in the core' pattern. Unlike machining-induced residual stresses that are typically confined to a shallow surface layer, quenching involves rapid cooling at the surfaces via intense heat transfer, while heat in the interior is removed more slowly by conduction to the surface. This temporal sequence creates a non-uniform temperature field and, owing to thermal expansion/contraction, a non-uniform thermal strain field that leads to the observed residual stress distribution.

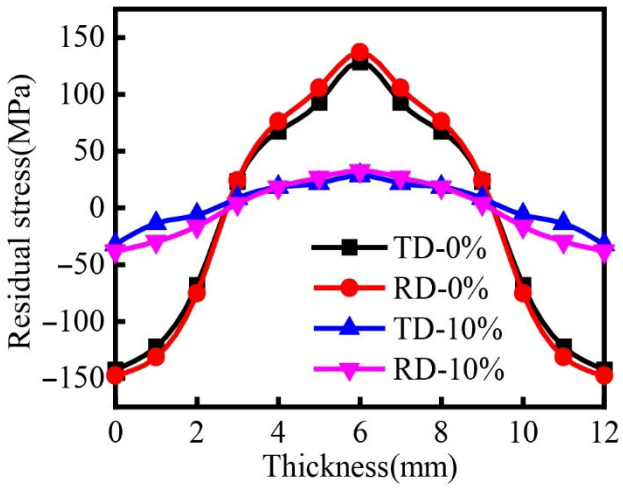


Figure 11. Through-thickness residual stress distributions after quenching and after pre-stretching.

After pre-stretching, the residual stress level decreases markedly, with the maximum compressive stress reduced from approximately −152 MPa to −48 MPa. This indicates that pre-stretching is effective in relieving residual stresses, consistent with previous findings.

4.3. Springback Prediction Accuracy Under Different Die Curvatures

Figure 12 compares the springback prediction errors of the NRS and RS models against experimental measurements for the original die configuration. The full-field error contour maps clearly show that the NRS model exhibits a wider deviation range (−1.69 to 7.90 mm), whereas the RS model significantly reduces the overall error distribution to −1.56 to 1.95 mm. Compared with the NRS model, the maximum deviation decreases by 6.08 mm. In terms of the error interval width, the prediction accuracy improves by approximately 63%, demonstrating the critical role of incorporating the initial residual stress field in CAF simulations.

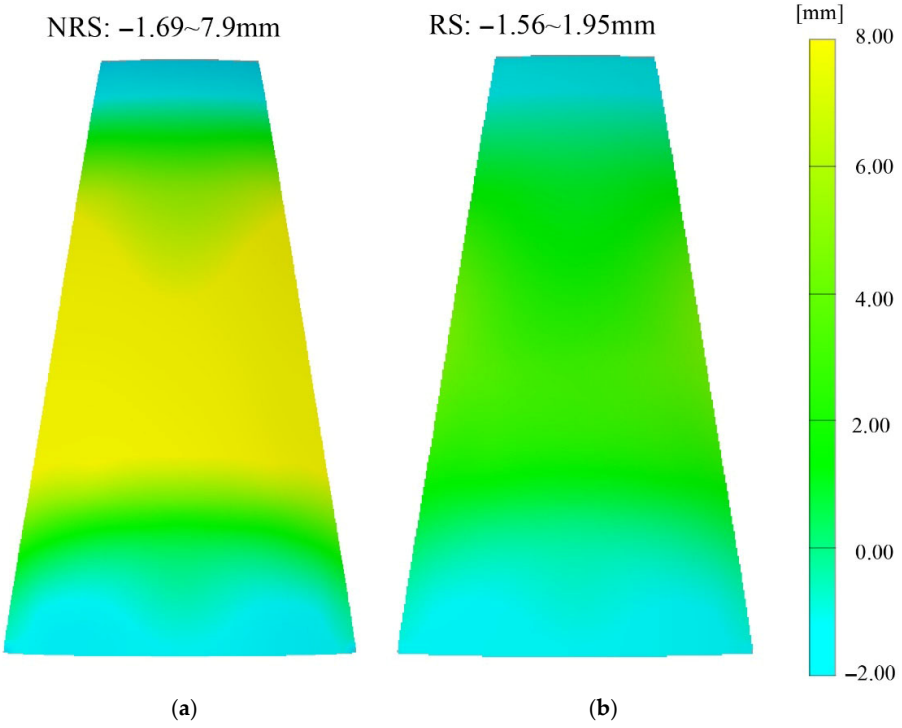


Figure 12. Springback prediction errors of the FE simulations compared with experimental measurements under the original die configuration: (**a**) NRS model; (**b**) RS model.

To further evaluate the robustness of the proposed modeling strategy, an additional die configuration with a shallower curvature was analyzed. The maximum geometric deviation between the shallow die and the original die was approximately 6 mm. For this configuration, the springback difference between the NRS and RS models, defined as

$$\Delta\text{springback} = \text{springback (NRS)} - \text{springback (RS)},$$

is illustrated in Figure 13.

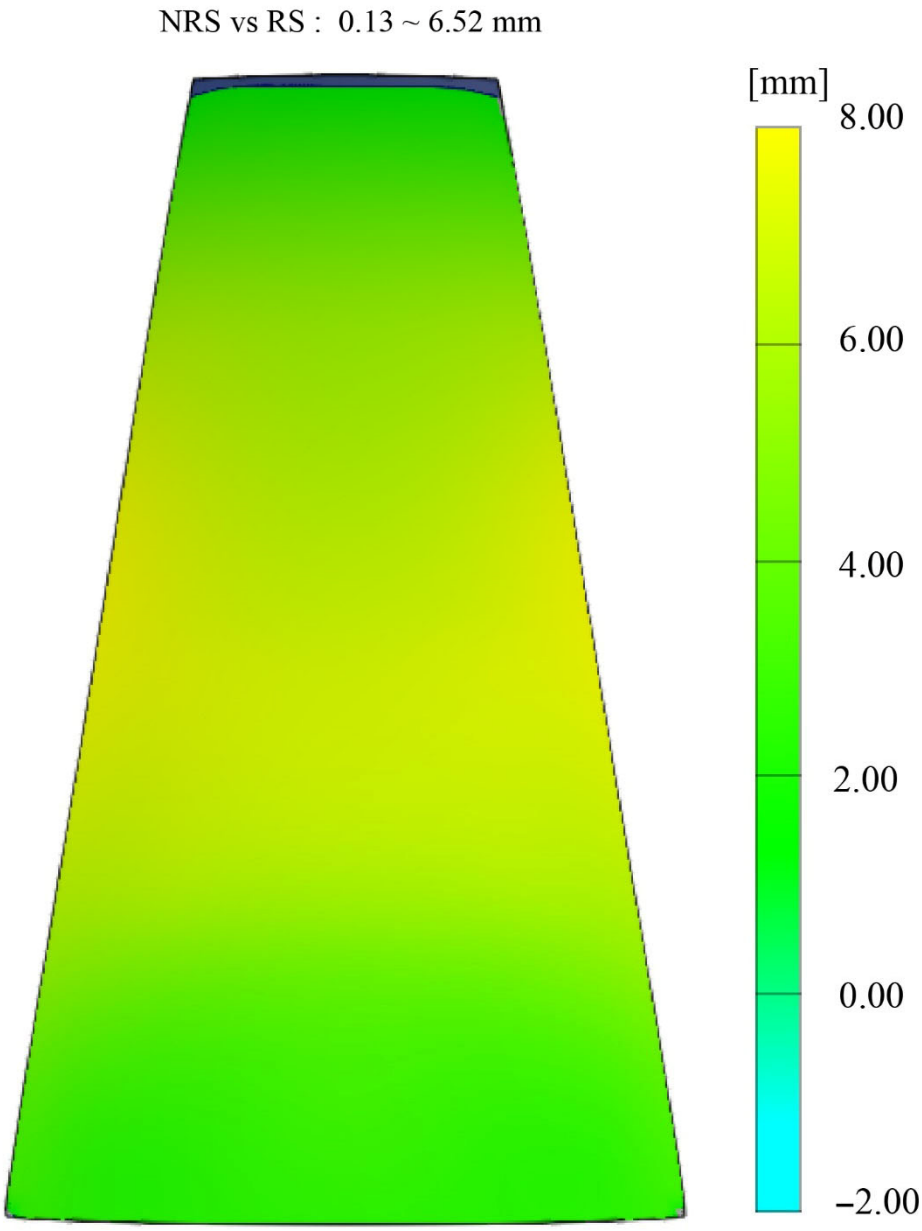


Figure 13. Distribution of springback difference (Δspringback = springback (NRS) – springback (RS)) under the shallower die configuration.

The Δspringback distribution under the shallower die condition ranges from 0.13 to 6.52 mm. For comparison, under the deeper (original) die configuration, the corresponding Δspringback range is −0.13 to 5.95 mm. Although minor local variations are observed due to geometric differences, the magnitude of springback reduction remains at the millimeter scale for both die curvatures.

A quantitative comparison of the error metrics under different die curvatures is summarized in Table 4. The results indicate that the improvement achieved by considering the initial residual stress field is consistent across different curvature levels.

Table 4. Quantitative comparison of springback prediction under different die curvatures.

Die Configuration	Error Range (NRS vs. Exp.) (mm)	Error Range (RS vs. Exp.) (mm)	ΔSpringback Deviation (mm) (Δ = Springback (NRS) – Springback (RS))
Experimental die	9.59 (−1.69 to 7.90)	3.51 (−1.56 to 1.95)	6.08 (−0.13 to 5.95)
Shallower die (deviation = 6 mm)	—	—	6.43 (0.09 to 6.52)

These findings demonstrate that the influence of the initial residual stress field on springback is not limited to a single die geometry. The proposed multi-step FE process chain maintains a stable predictive enhancement under varying curvature conditions, suggesting a certain degree of generality for practical CAF applications.

4.4. Stress and Strain Evolution

Figures 14–16 show the principal stress distributions on the mid-plane at different stages of CAF. Due to structural equilibrium, the stress difference caused by the initial residual stress field (≈40 MPa) decreases to within 10 MPa after the loading stage. After creep ageing, the stress distributions become almost identical. After springback, the principal stress on the mid-plane in the RS model is slightly higher than that in the NRS model.

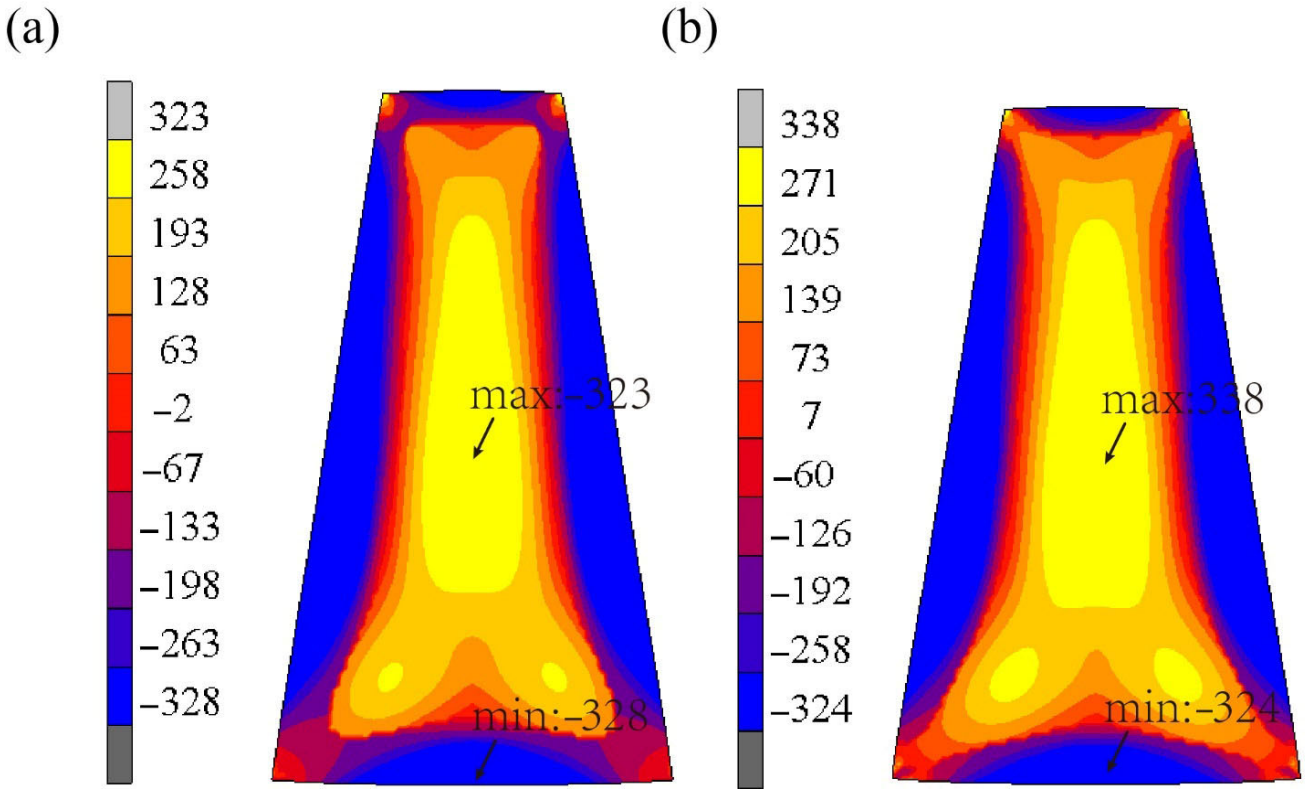


Figure 14. Principal stress distribution after loading: (**a**) NRS; (**b**) RS.

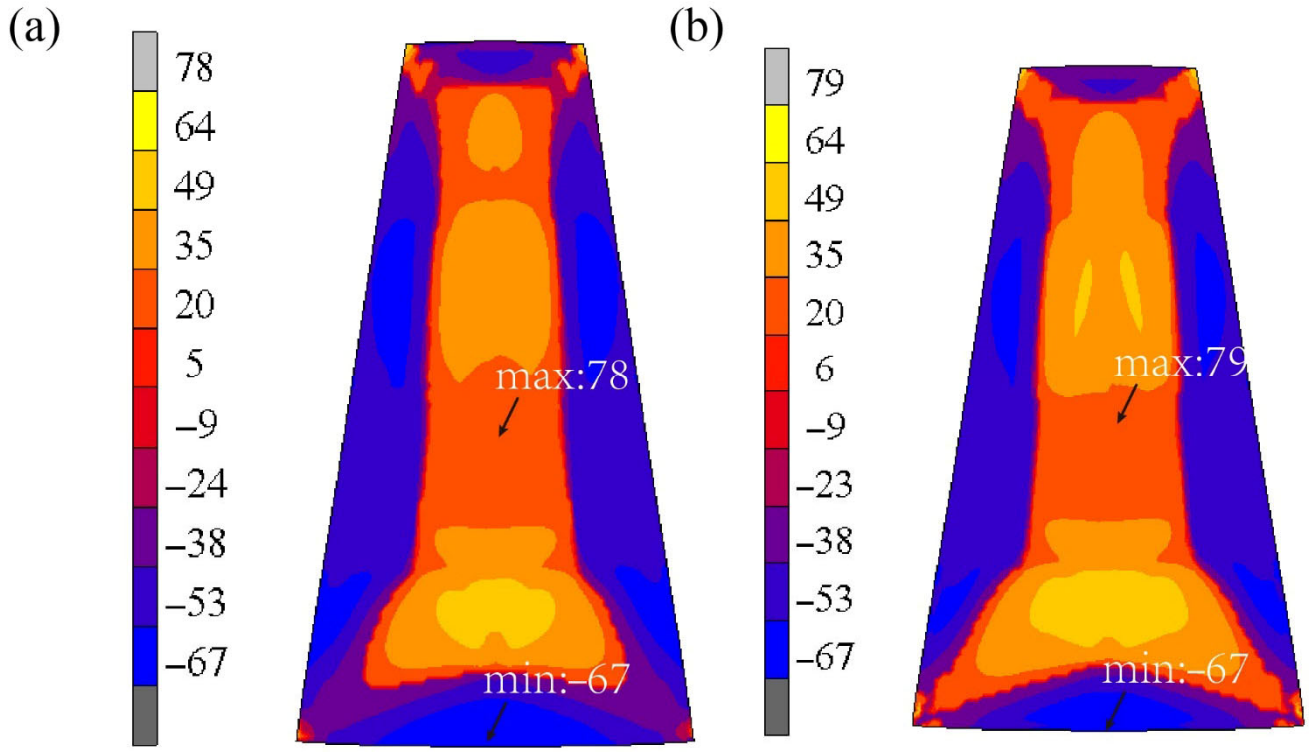


Figure 15. Principal stress distribution after creep ageing: (**a**) NRS; (**b**) RS.

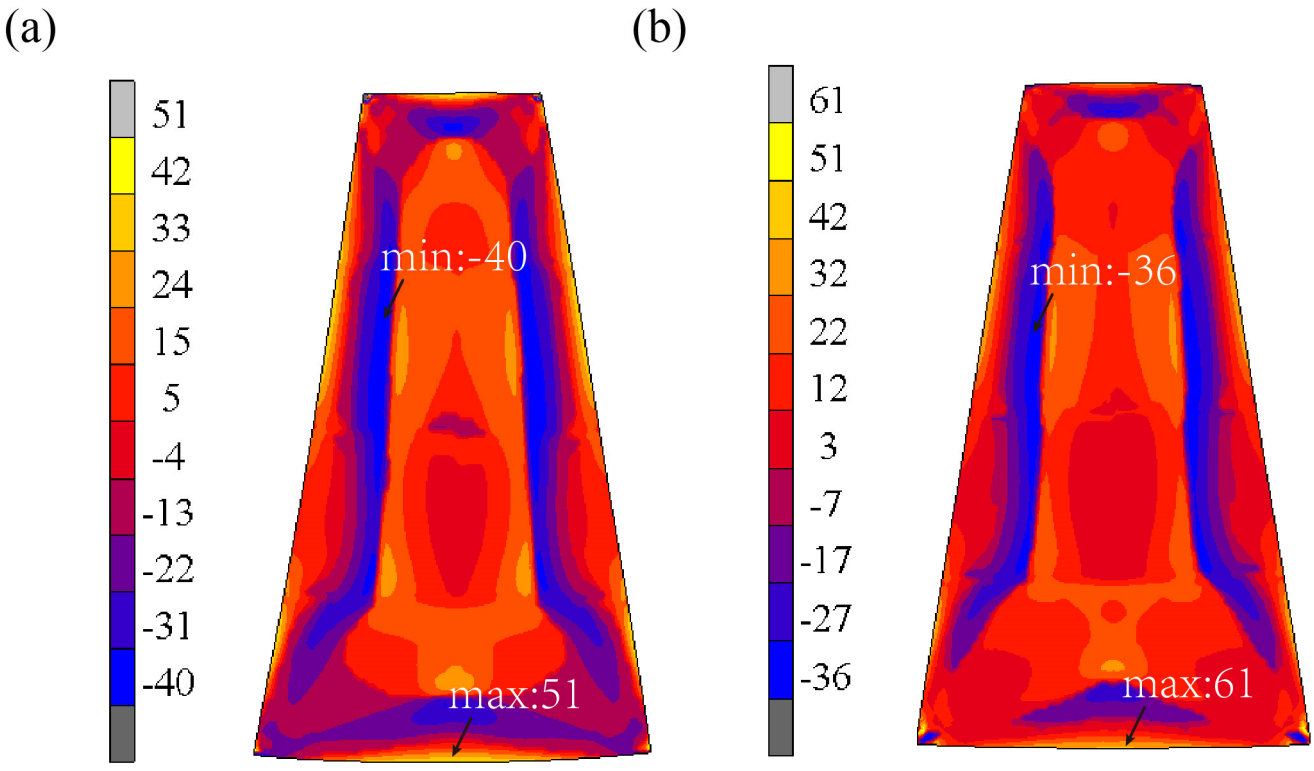


Figure 16. Principal stress distribution after springback: (**a**) NRS; (**b**) RS.

Figure 17 presents the stress distribution along Path A-A. After the loading stage, the stress in the RS model is significantly higher than that in the NRS model, whereas, after ageing and after springback, the stress values are nearly the same. This suggests that the springback difference may originate from two contributions: (1) differences in

plastic deformation during loading and (2) differences in accumulated creep deformation during ageing.

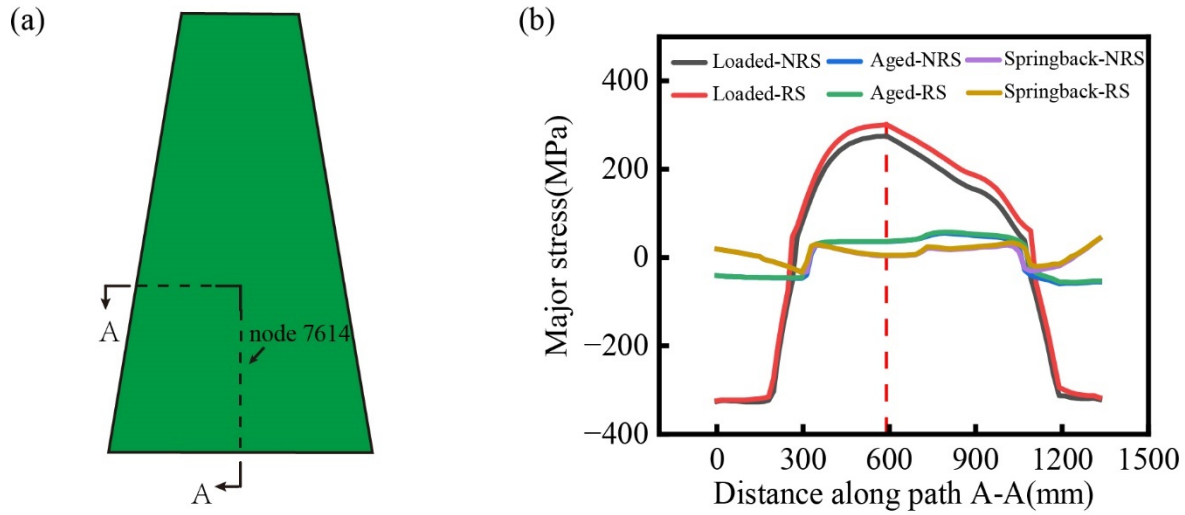


Figure 17. Stress distribution along Path A-A: (**a**) location of Path A-A; (**b**) principal stress distribution along the path. The dashed lines in (**b**) indicate the turning point of Path A-A shown in (**a**).

Figure 18a shows the distributions of plastic strain and creep strain along Path A-A. The plastic strain difference between the RS and NRS models is negligible. This is because the initial residual stress difference (≈40 MPa; Figure 11) is largely reduced during stress equilibration in the loading stage (Figure 14) and thus does not lead to an obvious plastic strain discrepancy. However, creep deformation accumulates iteratively over time. Even a small initial stress difference can result in an appreciable difference in creep strain (Figure 17b), leading to stabilized creep strains of ~0.15% (RS) and ~0.12% (NRS), which directly contributes to the difference in springback prediction accuracy.

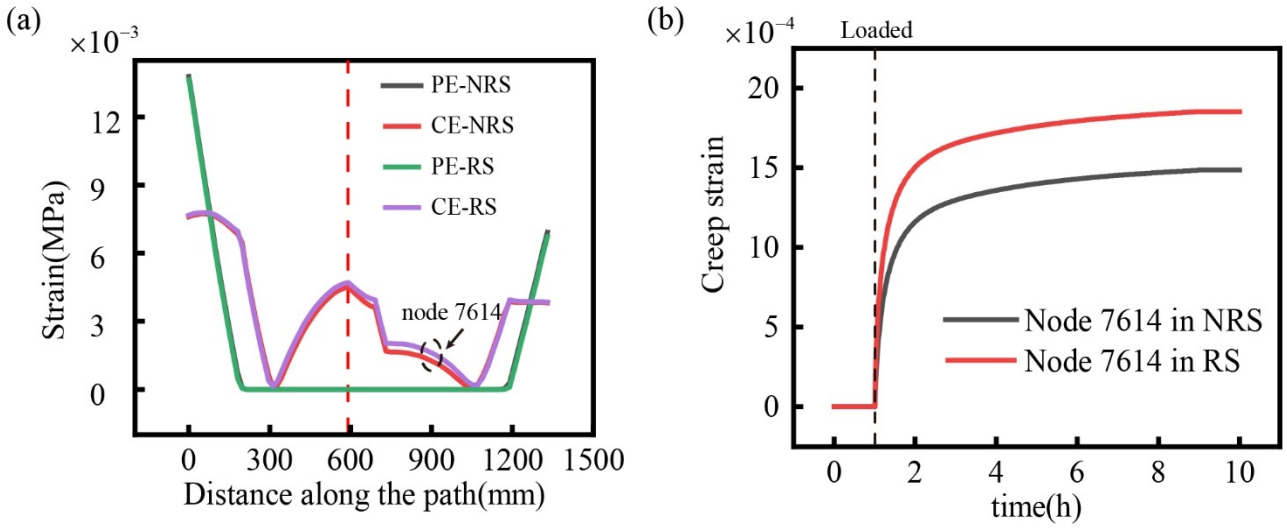


Figure 18. Inelastic deformation: (**a**) plastic and creep strains along Path A-A; (**b**) creep strain evolution at Node 7614. The dashed line in (**a**) indicates the turning point of Path A-A, while the dashed line in (**b**) marks the beginning of the creep stage.

The stress evolution characteristics observed above were also found to be consistent under the shallower die configuration. Although the absolute stress magnitude varies slightly due to geometric differences, the overall trend remains unchanged: the initial residual stress difference is largely equilibrated during loading, while the accumulated creep

strain difference persists and ultimately governs the springback discrepancy. This consistency further supports the notion that the effect of the initial residual stress is governed by creep strain accumulation rather than the die geometry.

5. Conclusions

A multi-step FE process chain (quenching–pre-stretching–CAF) was established for an AA2219-C10Z propellant tank panel and validated by experiments. The residual stress distributions after quenching and pre-stretching were analyzed, and the influence of the resulting initial residual stress field on the springback of a doubly curved component was investigated. The following conclusions can be drawn.

(1) After quenching, the through-thickness residual stress exhibits a 'compressive at the surfaces and tensile in the core' distribution, with maximum tensile stress of about 154 MPa on the mid-plane. Pre-stretching effectively reduces the residual stress level; the maximum mid-plane tensile stress decreases to about 40 MPa. The multi-step FE model successfully captures the residual stress evolution during the pre-processing stages.

(2) During the creep age forming of doubly curved components, the initial residual stress field influences springback primarily through its effect on accumulated creep deformation rather than plastic deformation during loading. Although the initial stress difference is largely equilibrated in the loading stage, small differences persist in creep strain accumulation, which ultimately govern the final springback discrepancy.

(3) Incorporating the initial residual stress field into the CAF simulation improves the springback prediction accuracy by approximately 63% under the original die configuration. Additional simulations conducted under a shallower die curvature (with a geometric deviation of about 6 mm) show that the springback reduction remains at the millimeter scale (0.09–6.52 mm), indicating that the proposed modeling framework maintains a consistent predictive improvement under different curvature conditions.

(4) The results demonstrate that accounting for pre-processing-induced residual stresses is essential for high-accuracy springback prediction in CAF. The established multi-step FE process chain provides a physically consistent and transferable approach to analyzing residual stress effects in thin-walled aluminum alloy components.

Future work will extend the proposed framework to more complex geometries and explore its applicability to other aluminum alloy systems and thickness levels.

Author Contributions: Conceptualization, Y.Y.; methodology, J.Y. and L.Z.; software, J.Y.; validation, L.Z. and Y.Y.; formal analysis, J.Y.; investigation, J.Y.; resources, Y.Y.; data curation, J.Y.; writing—original draft preparation, J.Y.; writing—review and editing, L.Z. and Y.Y.; visualization, J.Y.; supervision, Y.Y.; project administration, Y.Y. All authors have read and agreed to the published version of the manuscript.

Funding: This research was funded by the National Natural Science Foundation of China (Nos. U2341273, 52205435, U22A20190), the Natural Science Foundation of Hunan Province (Nos. 2022JJ40621 and 2026JJ50175), and the Project of State Key Laboratory of Precision Manufacturing for Extreme Service Performance (No. ZZYJKT2025-04).

Institutional Review Board Statement: Not applicable.

Informed Consent Statement: Not applicable.

Data Availability Statement: The original contributions presented in this study are included in the article. Further inquiries can be directed to the corresponding author.

Conflicts of Interest: The authors declare no conflicts of interest.

References

1. Zhou, C.; Zhan, L.; Liu, C.; Huang, M. Dislocation density-mediated creep ageing behavior of an Al–Cu–Li alloy. *J. Mater. Sci. Technol.* **2024**, *174*, 204–217. [CrossRef]
2. Zhan, L.; Xie, H.; Yang, Y.; Zhao, S.; Chang, Z.; Xia, Y.; Zheng, Z.; Zhou, Y. Investigation on creep deformation and age strengthening behavior of 304 stainless steel under high stress levels. *Materials* **2024**, *17*, 642. [CrossRef]
3. Yang, Y.; Zhan, L.; Liu, C.; Wang, X.; Wang, Q.; Tang, Z.; Li, G.; Huang, M.; Hu, Z. Stress-relaxation ageing behavior and microstructural evolution under varying initial stresses in an Al–Cu alloy: Experiments and modeling. *Int. J. Plast.* **2020**, *127*, 102646. [CrossRef]
4. Liu, C.; Yang, J.; Ma, P.; Ma, Z.; Zhan, L.; Chen, K.; Huang, M.; Li, J.; Li, Z. Large creep formability and strength–ductility synergy enabled by engineering dislocations in aluminum alloys. *Int. J. Plast.* **2020**, *134*, 102774. [CrossRef]
5. Yang, Y.; Zhan, L.; Shen, R.; Liu, J.; Li, X.; Huang, M.; He, D.; Chang, Z.; Ma, Y.; Wan, L. Investigation on the creep-age forming of an integrally-stiffened AA2219 alloy plate: Experiment and modeling. *Int. J. Adv. Manuf. Technol.* **2018**, *95*, 2015–2025. [CrossRef]
6. Yang, Y.; Zhan, L.; Shen, R.; Yin, X.; Li, X.; Li, W.; Huang, M.; He, D. Effect of pre-deformation on creep age forming of 2219 aluminum alloy: Experimental and constitutive modelling. *Mater. Sci. Eng. A* **2017**, *683*, 227–235. [CrossRef]
7. Xiong, Y.; Yang, Y.; Xie, H.; Zhan, L. Effect of ageing temperature on the mechanical properties and microstructures of cryogenic-rolled 2195 Al–Cu–Li alloy. *Mater. Sci. Eng. A* **2025**, *924*, 147855. [CrossRef]
8. Yang, Y.; Zhan, L.; Ma, Q.; Feng, J.; Li, X. Effect of pre-deformation on creep age forming of AA2219 plate: Springback, microstructures and mechanical properties. *J. Mater. Process. Technol.* **2016**, *229*, 697–702. [CrossRef]
9. Zhan, L.; Tan, S.; Yang, Y.; Huang, M.; Shen, W.; Zhao, X. A research on the creep age forming of 2524 aluminum alloy: Springback, mechanical properties, and microstructures. *Adv. Mech. Eng.* **2014**, *2014*, 707628. [CrossRef]
10. Abvabi, A.; Rolfe, B.; Hodgson, P.D.; Weiss, M. The influence of residual stress on a roll forming process. *Int. J. Mech. Sci.* **2015**, *101*, 124–136. [CrossRef]
11. Sedeh, M.R.N.; Ghaei, A. The effects of machining residual stresses on springback in deformation machining bending mode. *Int. J. Adv. Manuf. Technol.* **2021**, *114*, 1087–1098. [CrossRef]
12. Zhang, M.; Li, D. Theoretical and experimental investigation of the deformation shape in press-braking bending considering surface residual stresses induced by milling operation. *Int. J. Adv. Manuf. Technol.* **2024**, *131*, 1059–1069. [CrossRef]
13. Zhang, M.; Tian, X.; Wang, G. Residual stress analysis and its effect on springback for multi-step press-brake bending. *Proc. Inst. Mech. Eng. Part B J. Eng. Manuf.* **2023**, *237*, 1787–1797. [CrossRef]
14. Lam, A.C.L.; Shi, Z.; Lin, J.; Huang, X. Influences of residual stresses and initial distortion on springback prediction of 7B04-T651 aluminium plates in creep-age forming. *Int. J. Mech. Sci.* **2015**, *103*, 115–126. [CrossRef]
15. Li, Y.; Gan, W.; Huang, X.; Zhang, Y.; Zhou, W.; Li, D.; Zeng, Y. A quantitative study of machining-induced residual stress and its effect on subsequent creep age forming of aluminium alloy panels. *J. Mater. Process. Technol.* **2023**, *321*, 118147. [CrossRef]
16. Li, Y.; Shi, Z.; Lin, J.; Yang, Y.-L.; Saillard, P.; Said, R. Effect of machining-induced residual stress on springback of creep age formed AA2050 plates with asymmetric creep-ageing behaviour. *Int. J. Mach. Tools Manuf.* **2018**, *132*, 113–122. [CrossRef]
17. Salvatore, F.; Halila, F.; Mabrouki, T.; Hamdi, H. Numerical and experimental study of residual stress induced by machining process. *Int. J. Surf. Sci. Eng.* **2012**, *6*, 136–147. [CrossRef]
18. Acquesta, A.; Monetta, T.; Franchitti, S.; Borrelli, R.; Viscusi, A.; Perna, A.S.; Penta, F.; Esposito, L.; Carrino, L. Green electrochemical polishing of EBM Ti6Al4V samples with preliminary fatigue results. *Int. J. Adv. Manuf. Technol.* **2023**, *126*, 4269–4282. [CrossRef]
19. Viscusi, A. Numerical investigations on the rebound phenomena and the bonding mechanisms in cold spray processes. In *AIP Conference Proceedings*; AIP Publishing LLC: Melville, NY, USA, 2018; Volume 1960, p. 100017.
20. Viscusi, A.; Astarita, A.; Genna, S.; Leone, C. On the influence of different superficial laser texturing on the deposition of powders through cold spray process. *Trans. IMF* **2018**, *96*, 34–40. [CrossRef]
21. Wang, H.; Tong, R.; Liu, G.; Sha, A.; Song, L.; Zhang, T. In-Situ Synchrotron HEXRD Study on the Micro-Stress Evolution Behavior of a Superalloy during Room-Temperature Compression. *Materials* **2023**, *16*, 3761. [CrossRef]
22. Selbmann, R.; Gibmeier, J.; Simon, N.; Kräusel, V.; Bergmann, M. Residual Stress Engineering for Wire Drawing of Austenitic Stainless Steel X5CrNi18-10 by Variation in Die Geometries—Effect of Drawing Speed and Process Temperature. *Materials* **2024**, *17*, 1174. [CrossRef]
23. Liu, M.; Tao, X.; Di, Z.; Qin, M.; Liu, Z.; Bai, S. Effect of Pre-Rolling on Microstructure and Fatigue Crack Propagation Resistance of a Third-Generation Al–Li Alloy. *Materials* **2023**, *16*, 7540. [CrossRef] [PubMed]
24. Zeng, H.; Shi, D.; Zheng, Y.; Zhang, J. Effect of the Second Phases on Composite Spinning-Extrusion Forming and Mechanical Properties of Al–Cu–Li Alloy. *Materials* **2023**, *16*, 3573. [CrossRef] [PubMed]
25. Chen, Z.; Duan, Y.; Wang, P.; Qian, H. Residual Stress Redistribution Analysis in the Repair Welding of AA6082-T6 Aluminum Alloy Joints: Experiment and Simulation. *Materials* **2022**, *15*, 6399. [CrossRef] [PubMed]
26. Aubert & Duval. *Aluminium Alloy 2219 Datasheet*; Aubert & Duval: Paris, France, 2024.

27. Withers, P.J.; Bhadeshia, H.K.D.H. Residual stress. Part 1—Measurement techniques. *Mater. Sci. Technol.* **2001**, *17*, 355–365. [CrossRef]
28. Fitzpatrick, M.E.; Fry, A.T.; Holdway, P.; Kandil, F.A.; Shackleton, J.; Suominen, L. *Determination of Residual Stresses by X-Ray Diffraction—Issue 2*; Measurement Good Practice Guide No. 52; National Physical Laboratory: Teddington, UK, 2005.
29. Mo, F.; Sun, G.; Li, J.; Zhang, C.; Wang, H.; Chen, Y.; Liu, Z.; Yang, Z.; Li, H.; Yang, Z.; et al. Recent Progress of Residual Stress Distribution and Structural Evolution in Materials and Components by Neutron Diffraction Measurement at RSND. *Quantum Beam Sci.* **2018**, *2*, 15. [CrossRef]

Disclaimer/Publisher's Note: The statements, opinions and data contained in all publications are solely those of the individual author(s) and contributor(s) and not of MDPI and/or the editor(s). MDPI and/or the editor(s) disclaim responsibility for any injury to people or property resulting from any ideas, methods, instructions or products referred to in the content.